AAS 24-443

OBSERVING THE CISLUNAR SURVEILLANCE CONE FROM SYNODIC RESONANT ORBIT CONSTELLATIONS

Noah I. Sadaka[*], Maaninee Gupta[†], Kathleen C. Howell[‡], and Carolin Frueh[§]

Space situational awareness is a priority to enable the development of the cislunar region. The 30-degree cone with vertex at the Earth and opening towards the Moon is identified as a region requiring frequent visibility. Constellations of sidereal resonant orbits with a synodic resonance overlap in the Circular Restricted Three-Body Problem possess repeating geometries with the Sun and the surveillance cone. Different relative magnitude models are evaluated to examine their impact on observing objects of different radii. Visibility of the interior cone by a constellation is examined to evaluate the constellation surveillance characteristics.

INTRODUCTION

Sufficient space situational awareness to permit comprehensive space domain awareness of the cislunar region is crucial for safely expanding spaceflight operations into this environment.[1,2] One area of particular interest is the "surveillance cone" with vertex at Earth opening up towards the Moon.[3] Surveilling this region from a variety of vantage points is critical as lunar backlighting hampers viewing for terrestrial observers.[4] Therefore, space-based assets, such as the upcoming Oracle-P mission,[5] are required to provide the necessary space situational awareness information to enable sustainable spaceflight in cislunar space.

Observing cislunar space for the purpose of space situational awareness is recently a focus as spacecraft begin operating in this domain. Holzinger et al. describe some of the major challenges with observing cislunar space from ground-based sensors and propose cislunar orbits as more appropriate surveillance vantage points.[6] Vendl & Holzinger define a 20-degree surveillance cone and identify the visibility within it at various relative magnitude limits from synodic-resonant Lagrange point orbits associated with L_1 and L_2.[7] Bhadauria et al. examine the visibility of the planar circular region spanning a range from LEO to regions beyond the lunar orbit from inertially-fixed locations in space and determine the visibility of this region by considering exclusion cones and apparent magnitude constraints.[8] Gupta et al. employ cislunar periodic orbits to observe the lunar vicinity and to transit between the lunar and Earth regions.[3] The same authors also leverage constellations

[*]Ph.D Student, School of Aeronautics and Astronautics, Purdue University, West Lafayette, IN, 47907; nsadaka@purdue.edu

[†]Ph.D Candidate, School of Aeronautics and Astronautics, Purdue University, West Lafayette, IN, 47907; gupta208@purdue.edu; currently Postdoctoral Researcher, Texas A&M University, College Station, TX 77843; maanineegupta@tamu.edu

[‡]Hsu Lo Distinguished Professor of Aeronautics and Astronautics, School of Aeronautics and Astronautics, Purdue University, West Lafayette, IN, 47907; Fellow AAS, Fellow AIAA; howell@purdue.edu

[§]Harold DeGroff Associate Professor of Aeronautics and Astronautics, School of Aeronautics and Astronautics, Purdue University, West Lafayette, IN, 47907; cfrueh@purdue.edu

of cislunar orbits to observe the surveillance cone and transmit data to Earth.[9] Gupta expands on this analysis by employing solar, lunar, and Earth exclusion cones to determine the visibility of cislunar orbits by a constellation.[10] Visonneau et al. also explore the use of constellations for observing the surveillance cone by constructing them with a genetic algorithm that optimizes the visibility for a defined apparent magnitude cutoff.[11] A framework for characterizing cislunar orbits by their suitability for tracking objects in other cislunar orbits is described by Baker-McEvilly et al.[12] This investigation contributes to cislunar space situational awareness by leveraging constellations of synodic resonant orbits in the Circular Restricted Three-Body Problem (CR3BP) for their ability to observe the surveillance cone. Metrics that incorporate both apparent magnitude of a target and the geometry of exclusion cones are developed to evaluate the capability of a constellation to view the surveillance cone volume.

DYNAMICAL MODELS

Several dynamical models are employed. The Circular Restricted Three-Body Problem (CR3BP) is leveraged for cislunar periodic orbit generation and analysis. The Bicircular Restricted Four-Body Problem (BCR4BP) is employed to locate the Sun in the CR3BP. Finally, solutions are transitioned to a High-Fidelity Ephemeris Model (HFEM); an N-body model with epoch-dependent planetary, lunar, and solar positions.

THE CIRCULAR RESTRICTED THREE-BODY PROBLEM

The CR3BP is a time-independent model that describes the motion of a particle with negligible mass, labeled P_3, in a gravitational potential formed by two spherically-symmetric massive bodies. In this model, the massive bodies, termed the primaries and denoted P_1 and P_2 for the larger and smaller mass, respectively, move in circular orbits about their common barycenter. Any CR3BP system is characterized by the mass ratio $\mu = \frac{M_2}{M_1+M_2}$ for the primaries, where M_1 and M_2 are the masses of P_1 and P_2, respectively. Motion in this model is expressed in a barycenter-centered frame that rotates with the primaries as viewed in teal in Figure 1(a), with the right handed-triad $\hat{x}, \hat{y}, \hat{z}$ (carets identify vectors of unit length). The orientation of the rotating frame with respect to an inertial frame at a certain time is defined by the angle θ in Figure 1(a). The CR3BP equations of motion are non-dimensionalized by the distance between the primaries l^*, the total mass of the system, $m^* = M_1 + M_2$, and the characteristic time t^* that is selected such that the mean motion $\dot{\theta}$ for the primaries relative to the barycenter B, is equal to 1. The resulting equations of motion for the six-dimensional state for P_3, $\vec{r} = [x, y, z, \dot{x}, \dot{y}, \dot{z}]$, are

$$\ddot{x} = 2\dot{y} + \Omega_x \qquad (a) \qquad \ddot{y} = -2\dot{x} + \Omega_y \qquad (b) \qquad \ddot{z} = \Omega_z \qquad (c) \tag{1}$$

where Ω_i is a partial derivative of the pseudo-potential function Ω with respect to each of the position components, i: $\Omega = \frac{1-\mu}{\|\vec{r}_{13}\|} + \frac{\mu}{\|\vec{r}_{12}\|} + \frac{x^2+y^2}{2}$, and as evident in Figure 1(a), $\vec{r}_{12}$ and $\vec{r}_{13}$ are the respective position vectors from P_1 and P_2 to P_3. Arrow overbars indicate vectors.

The equations of motion admit five equilibrium solutions in the $\hat{x}-\hat{y}$ plane, denoted the Lagrange points. The collinear Lagrange points, i.e., L_1, L_2, and L_3, are all located along the $\hat{x}$-axis. The equilateral Lagrange points L_4 and L_5 form equilateral triangles with the primaries. No analytical solution in the CR3BP exists, however, one integral of the motion is available i.e., the Jacobi Constant (JC). This integral represents an energy-like quantity that remains constant along any ballistic arc and is evaluated for any state as $JC = 2\Omega - (\dot{x}^2 + \dot{y}^2 + \dot{z}^2)$.

Modeling the Sun in the Coplanar Bicircular Restricted Four-Body Problem

The coplanar BCR4BP is leveraged to locate the Sun in the CR3BP Earth-Moon rotating frame. As with the CR3BP, the Earth (P_1) and Moon (P_2) move in circular orbits around their common barycenter B. The Sun, denoted P_S, is assumed to follow a circular orbit about the $P_S - B$ barycenter B_S; B also follows a circular path around B_S. For the coplanar BCR4BP, the $P_1 - P_2$ and the $P_S - B$ orbital planes are not inclined relative to each other. The equations of motion for the BCR4BP are equivalently expressed in two frames; the Earth-Moon rotating frame and the $P_S - B$ rotating frame. As the solar location from the BCR4BP is modeled in the CR3BP Earth-Moon rotating frame, only the Earth-Moon rotating frame formulation is incorporated. Relevant quantities are the non-dimensional solar mass m_s; the mass of the Sun divided by the Earth-Moon mass parameter m^*, as well as the non-dimensional solar distance a_s; the average $P_S - B$ distance divided by l^*. The mean motion $\dot{\theta}_{SB}$ of the Sun as viewed in the Earth-Moon rotating frame is computed as $\dot{\theta}_{SB} = \sqrt{\frac{m_s+1}{a_s^3}} - 1$[13] where the resulting mean motion is negative as Sun travels around the Earth-Moon system clockwise. The CR3BP is employed for the orbit propagation, that is, the solar gravity is not incorporated; a reasonable assumption for the interior Earth-Moon system as the solar gravity is not a key force.[14] However, the location of the sun is obtained from the BCR4BP when evaluating the visibility of a location in space. From an initial solar position, the subsequent solar locations are computed for each time-step in the CR3BP propagation post-priori from this initial condition and the solar mean motion.

High-Fidelity Ephemeris Model

Solutions from the CR3BP are transitioned to the HFEM to evaluate their feasibility in this model that incorporates epoch-dependent positions for the bodies that describes their true motion. This model is constructed as an N-body model in an inertial frame from the relative position vectors $\vec{r}_{m,n} = \vec{r}_n - \vec{r}_m$ of the N bodies with respect to each other and the central body. For this investigation of cislunar resonant orbits, the Earth is selected as the central body, and therefore, the Earth-centered J2000 inertial frame is employed to describe the positions of the bodies and the spacecraft. A schematic of a HFEM model appears in Figure 1(b). The motion of the spacecraft $\vec{r}_{s/c,o}$ with respect to the central body P_o is described by the second-order system of equations that are non-dimensionalized by the Earth-Moon CR3BP characteristic quantities

$$\ddot{\vec{r}}_{o,s/c} = -\frac{m_o}{\|\vec{r}_{o,s/c}\|^3}\vec{r}_{o,s/c} - \sum_{\substack{j=1 \\ j\neq o,s/c}}^{N} m_j \left(\frac{\vec{r}_{j,s/c}}{\|\vec{r}_{j,s/c}\|^3} + \frac{\vec{r}_{o,j}}{\|\vec{r}_{o,j}\|^3} \right) \tag{2}$$

where m_j describes the mass of body P_j and the gravitational constant $G_{nd} = 1$ in this non-dimensional formulation of the equations. The planetary, lunar, and solar positions with respect to the Earth are retrieved from the DE440 ephemerides[15] provided by the NASA Jet Propulsion Lab's Navigation and Ancillary Information Facility.[16] The SPICE toolkit[17,18] is employed to extract the relevant relative position vectors required to evaluate Equation (2). An arbitrary number of perturbing bodies may be included in the HFEM, however, when focusing on the cislunar regime, incorporating the perturbing gravitational effects of the Moon, Sun, and Jupiter is reasonable.[10]

PERIODIC ORBITS IN THE CR3BP

Periodic solutions exist in the CR3BP as closed trajectories with some period, T. This repeatable motion is frequently leveraged when designing trajectories to provide structure in an otherwise

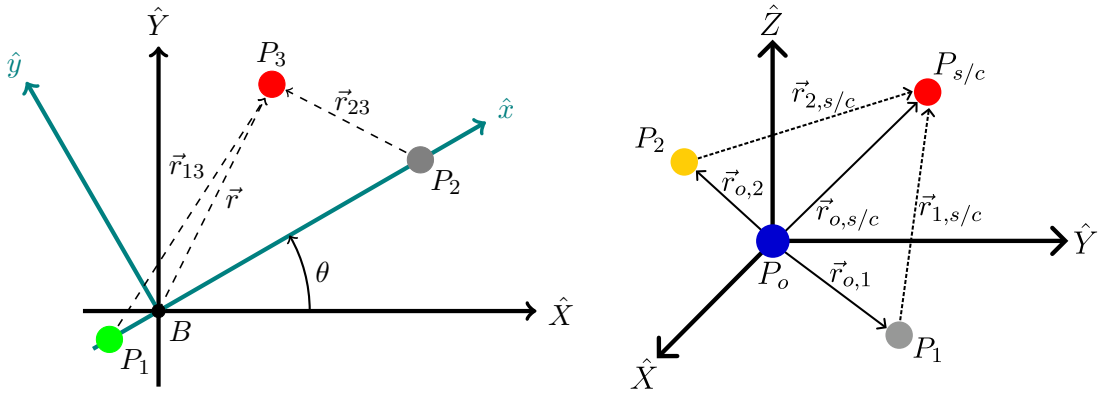

(a) The CR3BP rotating frame.

(b) Schematic for an Earth-centered $N = 4$ ephemeris model.

Figure 1: Model frameworks.

complex dynamical environment. These solutions also serve as an initial guess when transitioning to the HFEM; additional operational constraints such as eclipse avoidance may also be included while preserving the CR3BP orbital geometry.[19–21] Periodic orbits are constructed from an initial guess for a state vector, propagating, and employing a corrections algorithm to deliver periodicity. Families of periodic orbits are expanded from the corrected solution by varying one or several orbital parameters and re-correcting the trajectory to be periodic.

Periodic orbits are often characterized by their stability properties. The state transition matrix for a periodic orbit evaluated after precisely one period, termed the monodromy matrix, possesses an eigenstructure that informs on the linear stability properties of the orbit. Due to the hamiltonian structure, the eigenvalues are in reciprocal pairs. Then, an orbit whose monodromy matrix has at least one eigenvalue with real part greater than 1 is denoted a linearly unstable orbit; an orbit is considered marginally linearly stable if all eigenvalues lie on the unit circle. Several metrics for quantifying the stability of an orbit exist. The maximum stability index, often evaluated as $\nu = \max(0.5(\|\lambda_i\| + 1/\|\lambda_i\|))$,[22] where λ_i are the eigenvalues, is one suitable metric for evaluating stability, however it is not appropriate when comparing the stability of orbits with different periods due to the inflation in the magnitude of the eigenvalues as the time-of-flight of an orbit increases.[23] Instead, the time constant κ_T is selected for evaluating stability, and is defined as $\kappa_T = \frac{T}{\ln(\max(\lambda_i))}$, where κ_T describes the amount of time required for a perturbation from the reference motion to grow by a factor of e and T is the period.[22] This metric is therefore well-suited to compare stability information between orbits, as it directly relates the "departure" from the orbit in terms of time and operationally, is related to the frequency of stationkeeping maneuvers required to maintain the reference motion.

Sidereal Resonant Orbits

Sidereal resonant orbits are a classification of periodic orbits in the CR3BP that are characterized by a $p : q$ resonance ratio where, in the Earth-Moon system, p represents the number of revolutions of the orbit around the Earth as viewed in an Earth-centered inertial frame and q is the corresponding number of revolutions of the Moon around the Earth in approximately the same time.[24] The numerous possible resonance ratios define a large set of resonant orbit families that possess varied geometries that collectively reach many useful locations throughout the Earth-Moon space, such as

the regions near the primaries, the vicinities of the Lagrange points, and the exterior region of the system.[25] From the set of possible resonant orbit families, specific orbits are selected to satisfy a particular set of mission objectives.

Periodic orbits appear as planar or spatial families. Two types of spatial families are identified by their symmetry across the x-axis: PC-type families possess mirror configurations with *perpendicular crossings*, i.e. a state vector of the form $\vec{x} = \begin{bmatrix} x & 0 & z & 0 & \dot{y} & 0 \end{bmatrix}$, while AC-type families possess *axial crossings* with a state vector of form $\vec{x} = \begin{bmatrix} x & 0 & 0 & 0 & \dot{y} & \dot{z} \end{bmatrix}$. The 3:2 planar sidereal resonant orbit family plotted in Figure 2(a) is identified as possessing a geometry with apses in the lunar vicinity, and these characteristics are noted to persist for the associated PC-type spatial family plotted in Figure 2(b) and the AC-type family plotted in Figure 2(c). These spatial orbits host constellations of observers to view this region, as the particular 3:2 geometry offers multiple vantage points that linger near the region of interest for extended time intervals.

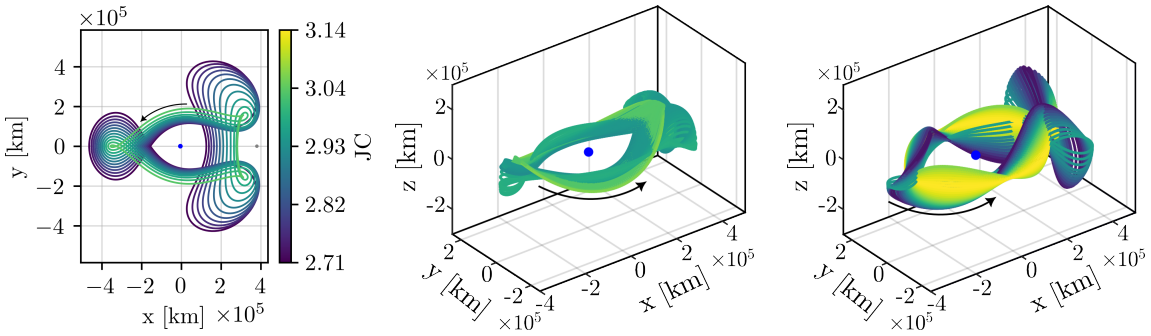

(a) Planar. (b) Spatial PC-type. (c) Spatial AC-type.

Figure 2: Subsets of the 3:2 spatial and planar sidereal resonant orbit families. The color scale is consistent across the three families.

CONSTELLATIONS OF SYNODIC RESONANT ORBITS

Orbits possessing a period that is commensurate with the synodic period, i.e., the time for the Earth-Moon-Sun configuration to repeat, are synodic resonant. This resonance is notably different from sidereal resonance, even though both are described by similar nomenclature. Sidereal resonance is defined by a $p : q$ integer ratio, and are described in an Earth-centered inertial frame. For example, a precisely $3 : 4$ resonant orbit possesses a period of $T_{inertial} = 4/3T_{sidereal}$ to yield a closed path in the inertial frame, however, it requires 3 revolutions in this inertial frame, corresponding to 4 lunar revolutions, to be closed in the rotating frame, and therefore, its period in the rotating frame is actually $T = 4T_{sidereal}$. In contrast, synodic resonances are also defined by a $p : q$ integer ratio, but this ratio describes orbital revolutions as viewed in the *rotating frame*. Now considering a $3 : 4$ synodic resonant orbit, it possesses a period of $T = 4/3T_{synodic}$ when viewed in the rotating frame. The synodic resonance ratio instead delivers the number of revolutions of the orbit in the rotating frame to yield q synodic periods. While this orbit may not be closed when viewed in the inertial frame, these 3 revolutions of the orbit in the rotating frame result in a total time of flight of $4T_{synodic}$ in the inertial frame. This information is summarized in Table 1.

As the definitions for sidereal and synodic resonant orbits are distinct, sidereal resonant orbits that possess synodic resonant periods, termed orbits with a *sidereal-synodic resonance overlap*,[10]

exist. This feature is possible due to the periods of sidereal resonant orbits being near, but generally not exactly equal to, the sidereal resonant period. The orbital period therefore varies across the family, as is viewed for the spatial 3:2 sidereal resonant families in Figure 3. Selecting orbits with a sidereal-synodic resonance overlap permits leveraging the desired geometry from the sidereal resonant orbit family while maintaining repeatability with the Earth-Moon-Sun configuration.

Table 1: Comparison of synodic and sidereal resonance ratio definitions.

Resonance type	Rotating frame period	Inertial frame period
Sidereal $p:q$	$qT_{sidereal}$	$\frac{q}{p}T_{sidereal}$
Synodic $p:q$	$\frac{q}{p}T_{synodic}$	$qT_{synodic}$

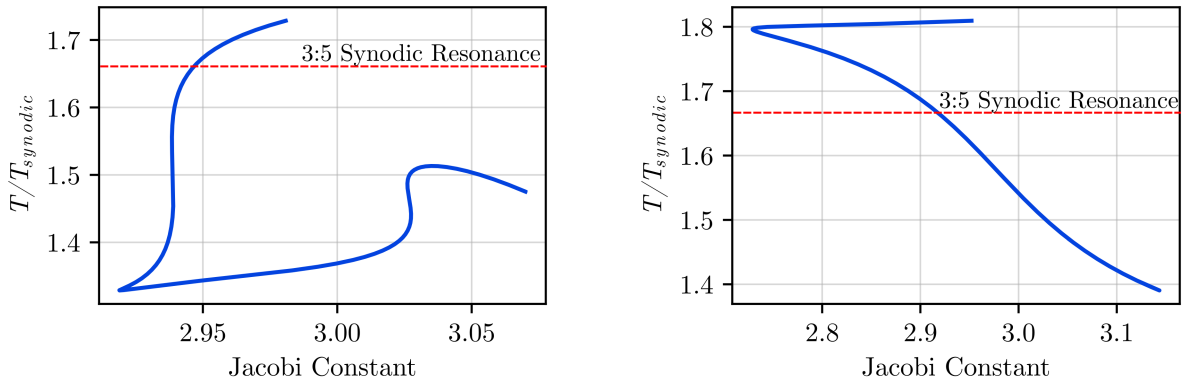

(a) PC-type family.

(b) AC-type family.

Figure 3: Variation in the fraction of an orbital period T with respect to a synodic period $T_{synodic}$ plotted against Jacobi Constant value for the spatial 3:2 sidereal resonant orbit families. The 3:5 synodic resonance value is highlighted by the dashed line.

Constellations (a number of satellites spaced along the orbit) are placed on synodic-resonant orbits such that the constellation configuration is also resonant with the synodic period. The location of a spacecraft along an orbit is parametrized by the encoding angle $\theta_{enc} = 2\pi t/T$ introduced by LaFarge and Howell,[26] where t is measured as the time of flight since departing the apse nearest to the Moon. Define a constellation of nq spacecraft equally-spaced in time along the same $p:q$ synodic resonant orbit, i.e. spaced by $\frac{T}{nq}$ in time along the orbit, where n is a non-zero integer. Each spacecraft rotates by $\theta_{enc} = 2\pi p/q$ increments along the orbit every synodic period, ensuring that some spacecraft are always located at the same encoding angle values as the configuration at the initial time. As a synodic resonant orbit is defined by two commensurate periods, the synodic period and the period of the orbit, the movement of spacecraft in the constellation are mapped to a torus, where the longitudinal angle represents the solar phase angle θ_{SB} and the latitudinal angle represents the encoding angle θ_{enc} for each spacecraft. Figure 4(a) plots the motion of a five-spacecraft constellation on a $3:5$ synodic resonant orbit, where the presence of closed curves indicates that the constellation configuration repeats. The configuration restoration is viewed on a stroboscobic map for the torus in Figure 4(a) after a synodic period, as illustrated in Figure 4(b).

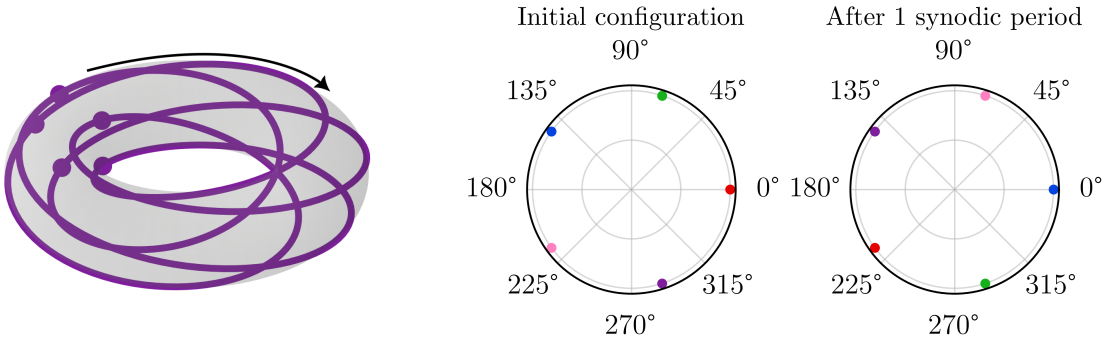

(a) Torus representing the solar phase angle (longitudinal angle) and spacecraft encoding angle (latitudinal angle).

(b) Stroboscopic mapping of the encoding angle for each spacecraft in the constellation at the initial time and after one synodic period. Note the rotation angle of $2\pi p/(nq)$.

Figure 4: Visualizing a five-spacecraft constellation placed along a $3:5$ synodic resonant orbit.

EVALUATING THE VISIBILITY OF THE SURVEILLANCE CONE

The surveillance cone, defined by a 30-degree half-angle with vertex at the Earth and directed towards the Moon, is identified as a region of interest for space situational awareness.[3,4] This cone angle is generally considered as the Lunar exclusion angle for observers on Earth's surface, where the background brightness of the atmosphere due to lunar backlighting limits optical observations. The cone extends to $\hat{x} = 500000$km, or approximately 55353km beyond the location of L_2. Within this cone, two sub-regions are identified. The first is a cone with a 10-degree half angle representing the lunar exclusion cone for Earth-orbiting observers. This lunar exclusion cone exists as an operational constraint for spacecraft with optical sensors, as a point angle that remains outside the exclusion cone prevents stray light reflected from the Moon from entering the sensor.[27] The second zone, denoted the L_1L_2 sphere, is centered around the Moon with a radius of 0.3 non-dimensional length units, or approximately 115424km, and approximately bounds the subset of the halo orbit families in the vicinity of L_1 and L_2, a region that is often the focus for cislunar trajectory design. This sphere is larger than the Moon Hill sphere of radius approximately 61175km, as the Hill sphere only extends to the L_1/L_2 libration points and does not capture portions of some of the halo orbits, most notably at their apolunes where observations would be most beneficial. These zones are viewed in Figure 5.

Apart from the lunar exclusion cone, space-based observers additionally consider solar and Earth exclusion cones to prevent stray light entry due these bright bodies.[28] The orientation of these exclusion zones are a function of both the observer position and the luminous bodies themselves. Lunar, solar, and Earth exclusion cones are incorporated, with half-angles of 10, 30, and 10 degrees, respectively.[10] The values of the exclusion cone angles are hardware-dependent for a given optical sensor design, however, this baseline set of exclusion angles permits a preliminary analysis considering generic space-based observers. As synodic resonant orbits are periodic with the Sun-Earth-Moon configuration, and the synodic resonant constellation configuration is maintained every synodic period, the lunar, solar, and Earth exclusion cones for the constellation also return to an initial orientation after this period.[8] A visibility analysis incorporating exclusion cones over a synodic period, therefore, informs on long-term visibility capabilities.

The relative magnitude of an object within the surveillance cone is also incorporated when evaluating the visibility. Assuming a single object, termed the point of interest (POI), its illumination is

computed via an illumination model; several formulations exist, and model selection has a crucial impact on the results of the visibility analysis. Generic objects in space are typically assumed to act as Lambertian spheres to simplify the analysis and to reduce the number of parameters required (including, for example, spacecraft attitude dynamics, specific geometry, and reflectivity coefficients of different surfaces); spacecraft are also most often composed of flat plates that reflect specularly. However, this approximation is often employed as the sphere exposes the same area to the Sun as the solar panels of a stabilized spacecraft.

Several spherical Lambertian illumination models exist; two are considered in this section to illustrate the impact of model selection. The relative magnitude of an object is evaluated via

$$m_{obj} = m_{sun-at-earth} - 2.5\log_{10}(I_{obj}/I_{sun-at-earth}) \tag{3}$$

where m refers to a magnitude, subscript obj to the object, and I to an irradiance. Differences between models typically lie in the definition for I_{obj}, where $I_{obj} = I_{sun-at-obj}\tau\Psi$.[29,30] The solar irradiance at the location of the object $I_{sun-at-obj}$ is scaled by the phase function Ψ that incorporates the geometry of the observer, the object, and the Sun to determine the quantity of light reflected back towards the observer. This quantity is further scaled by the travel function τ that describes the dispersion of the reflected light as it travels from the object to the observer. The resulting I_{obj} is the amount of light received by the observer from the object. The model leveraged in this investigation is described by Frueh et al.,[29,30] where the full magnitude expression is

$$m_{obj} = m_{sun-at-earth} - 2.5\log_{10}\left(\frac{r_{sun,obj}^2}{AU^2}\frac{1}{2\pi r_{obs,obj}^2}\left(\frac{2R_{obj}^2 C_d}{3\pi}(\sin\alpha + (\pi-\alpha)\cos\alpha)\right)\right) \tag{4}$$

where the first term in the log function scales the solar irradiance from the average Earth location at 1AU to the location of the object, the second term is the travel function for light distributed over a half sphere, and the third term is the phase function, where C_d is the Lambertian coefficient, R_{obj} the object radius, and α is the angle between the object, Sun, and observer. This formulation differs from the model introduced by Shell[31]

$$m_{obj} = m_{sun-at-earth} - 2.5\log_{10}\left(\frac{1}{r_{obj,obs}^2}\left(\frac{2(2R_{obj})^2 C_d}{3\pi}(\sin\alpha + (\pi-\alpha)\cos\alpha)\right)\right) \tag{5}$$

Apart from not scaling the solar irradiance to the object's location, Shell's formulation incorporates the surface area of the sphere as the reflecting area and, consequently, pairs it with a travel function more commonly employed for a flat plate. As a result, the Shell model estimates an object to be approximately 8π brighter than the Frueh model, corresponding to a magnitude difference of approximately -3.5. As is apparent later in the results, this difference significantly impacts the visibility of different size objects from cislunar constellations.

To assess the visibility of the surveillance cone regions, 100000 POIs are randomly sampled from a uniform distribution within the surveillance cone via rejection sampling, as plotted in Figure 5(b), and the visibility of each point is evaluated. For each POI at a particular epoch, the set of spacecraft that do not observe this point in an exclusion zone are recorded and the smallest magnitude for the POI as observed by this set is selected to represent the visible magnitude of the POI as seen by the constellation. When this minimum magnitude is larger than the cutoff magnitude of 20, selected as a baseline magnitude limit that is consistent with previous investigations,[7,10] or when the POI lies within the exclusion cones for all spacecraft in the constellation, the POI is described as not visible by the constellation. This process is repeated over a synodic period. Note that unless described otherwise, the Frueh model is employed when assessing the relative magnitudes.

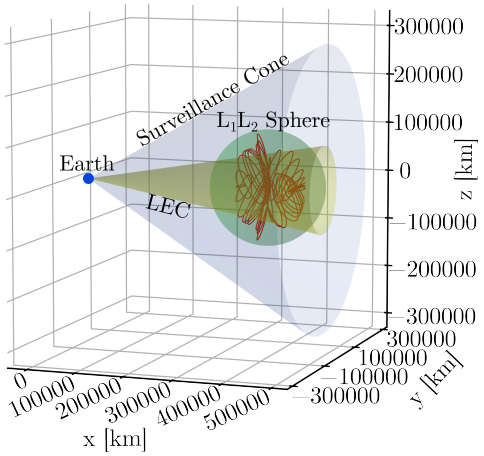

(a) Zones under consideration: the 30-degree surveillance cone, the 10-degree lunar exclusion cone (LEC) for observers near the Earth, and the L_1L_2 sphere. A subset of the northern and southern L_1 and L_2 halo families is plotted in red.

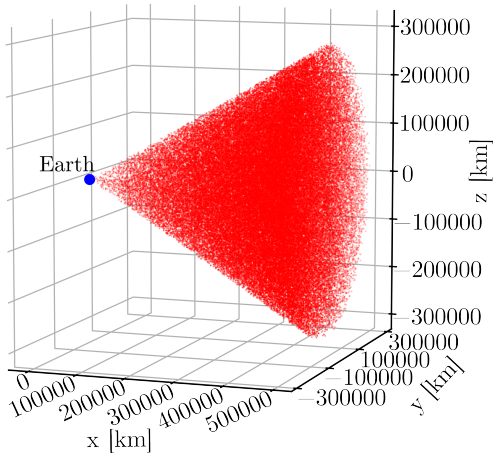

(b) A random uniform distribution of 100000 points within the surveillance cone.

Figure 5: Region of interest for cislunar SSA observations.

RESULTS: 1:1 SYNODIC RESONANT L_1 LYAPUNOV ORBIT

The 1:1 synodic resonant L_1 Lyapunov orbit is identified as a candidate orbit in a multi-orbit constellation of observers by Visonneau et al.[11] Vendl & Holzinger[7] also identify this orbit as a suitable path to place observers onto. The synodic resonant properties of this orbit provide repeating visibility characteristics for the surveillance region, the orbital geometry maintains the orbit within the surveillance cone for large intervals relative to the orbital period as apparent in Figure 6(a); and, as noted by Vendl & Holzinger, properly phasing an observer on this orbit with the Sun angle naturally aligns the viewing direction towards the cone with the incident solar rays such that objects in the cone are well-illuminated with respect to the observer.[7] Building from these contributions, a synodic-resonant constellation is investigated for this orbit. As this L_1 Lyapunov orbit possesses a 1:1 synodic resonance, an arbitrary number of spacecraft in the constellation return to a baseline configuration every synodic period. Several constellations are examined, and a four-spacecraft constellation yields high visibility of the cone employing all the spacecraft for objects at a given radius. Larger constellations result in diminishing returns in terms of surveillance cone visibility improvement.

The visibility of the points within the surveillance cone are analyzed by separately employing the magnitude models described by Frueh et al.[29,30] and Shell.[31] The analysis is accomplished out for objects with Lambertian coefficients of $C_d = 0.5$ and various radii, from $R_{obj} = 0.5m$ representing a generic multi-unit cubesat, to $R_{obj} = 3.5m$ representing a medium-to-large spacecraft of a similar size to the Gateway HALO module length. The initial solar phase angle is zero, i.e., the Sun initially lies on the positive $\hat{x}$-axis, and the encoding angle for one spacecraft is initially zero. The percentage of points within the surveillance cone that are visible by the constellation for one synodic period are plotted in Figures 6(b) and 6(c), where the solid lines represent the analysis results when employing the Frueh magnitude model and the dashed lines represent the results when employing the Shell magnitude model.

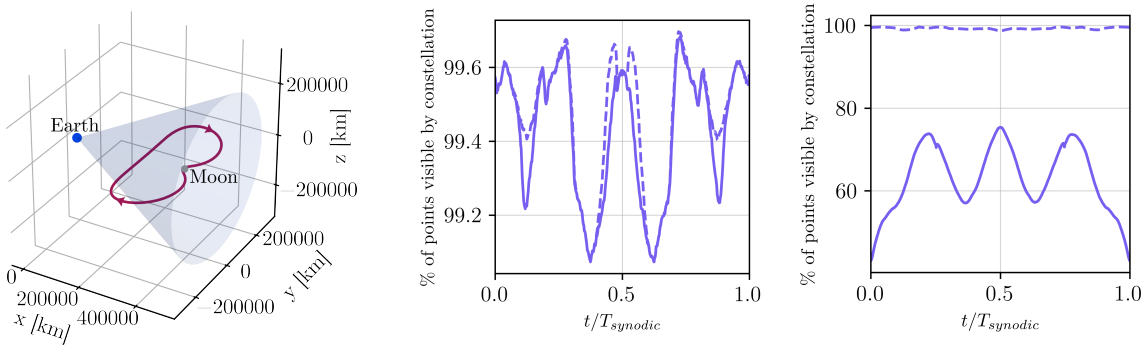

(a) 1:1 synodic resonant L_1 Lyapunov orbit and the surveillance cone region.

(b) $R_{obj} = 3.5m$

(c) $R_{obj} = 0.5m$.

Figure 6: b) and c): Percentage of points within the surveillance cone that are visible by the constellation for objects with a Lambertian coefficient of $C_d = 0.5$. Dashed lines represent the visibility when employing the magnitude model described by Shell,[31] and solid lines when employing the magnitude model described by Frueh et al.[29,30]

For the analysis employing the Frueh model, the reduction in radii significantly reduces the percentage of points in the surveillance cone that are visible by the constellation, as the magnitude cutoff of $m = 20$ increasingly reduces the set of points that are visible from the combined capabilities of the four spacecraft, until a drastic reduction in visible points occurs as the object radius drops to $R_{obj} = 0.5$. In contrast, the results that incorporate the Shell magnitude model are less dependent on the object radii for this magnitude cutoff. For the $R_{obj} = 3.5m$ case in Figure 6(b), the percentage of points visible by the constellation between the models is similar. However, the results employing the Shell model do not have any points with magnitude greater than 20; regions that are not visible by the constellation are limited only by the overlaps in exclusion cones from the constellation. For smaller radii, such as for $R_{obj} = 0.5m$ in Figure 6(c), the impact of the magnitude model on the visibility results is apparent. The percentage of points visible from the constellation when employing the Shell model is considerably higher than with the Frueh model. The large difference in the results between the two models highlights the importance of magnitude model selection and the assumptions incorporated. The challenges in observing the cislunar region are apparent; the brightness of objects under observation is a crucial parameter in cislunar SSA,[8] and understanding the reflection properties of these objects is necessary when designing the trajectories and hardware for observation.

This L_1 Lyapunov orbit is linearly unstable, with a time constant of $\kappa_T = 1.445$ non-dimensional time units or approximately 6.283 days, where time constant values less than 1.5 non-dimensional time units are sometimes considered to possess "fast" departure characteristics.[32] However, the geometry of this orbit when paired with a constellation of observers strategically phased in the orbit offer varied vantage points for regions within the cone, reducing the "blind spots" for the constellation. Additionally, the constellation remains in the vicinity of the cone for a large percentage of the orbit, contributing to the large number of points that are visible, as spacecraft do not spend time in other regions of space. However, should other regions of cislunar space be selected as regions of interest for SSA, such as the L_3 region, it would be challenging to view them due to the large distances of these regions from the L_1 Lyapunov orbit.

RESULTS: 3:5 SYNODIC RESONANT 3:2 SIDEREAL PC-TYPE SPATIAL RESONANT ORBIT

For observing the surveillance cone, several geometrical heuristics are noted to result in diverse vantage points of the surveillance cone region. Orbits possessing large $\hat{x}$-axis excursions limit the impact of the solar surveillance cone constraint when paired with a sufficient number of spacecraft in the constellation. Orbits with apoapses within the cone then result in several spacecraft in the constellation remaining in that region for long periods of time, providing various point of view that are near many of the points in the cone. The 3:2 spatial PC-type family is illustrated in Figure 2(b), and from the synodic ratios in the period variation across the family plotted in Figure 3(a), the 3:5 synodic member is selected as it possesses the desired geometrical properties and supports a synodic resonant constellation of $5n$ spacecraft; 5 spacecraft are selected for the particular constellation described in this section. This orbit is viewed in the CR3BP rotating frame in Figure 7. This orbit is linearly unstable, but less unstable than the 1:1 synodic L_1 Lyapunov orbit, with a time constant of $\kappa_T = 2.857nd$, or approximately 12.42 days, corresponding to around double the time constant of the Lyapunov orbit in the previous section.

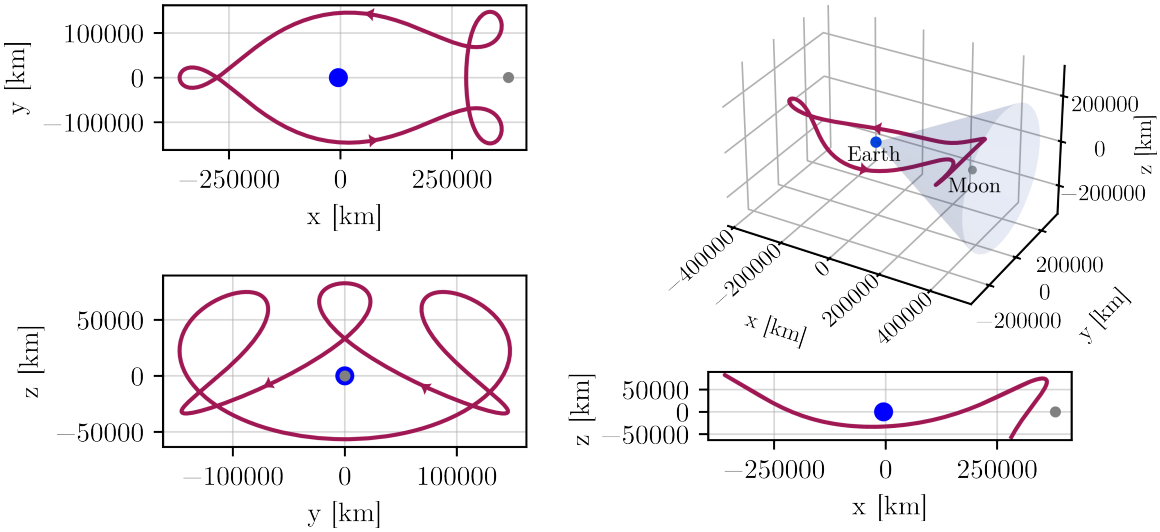

Figure 7: Views of the 3:2 spatial PC-type sidereal resonant orbit possessing 3:5 synodic resonance in the Earth-Moon CR3BP rotating frame. The surveillance cone is highlighted in the top-right isometric view.

The constellation is initially phased with a solar angle of zero and with one of the spacecraft at an encoding angle of zero. The results from the visibility analysis for this constellation are presented in Figure 8 for objects with radii of 0.5m, 1.5m, and 3.5m. The visibility characteristics of the orbit with objects of the largest radius, described in Figure 8(c), are primarily limited by exclusion zone constraints, however the geometry of the orbit with this constellation results in a high percentage of the cone being visible, with average percentages of points visible by the constellation of 99.0%, 97.4%, and 98.7% for the 30-degree surveillance cone, 10-degree lunar exclusion cone, and L_1L_2 sphere, respectively.

With smaller radius objects, the visible magnitude cutoff of $m = 20$ reduces the number of points visible in the regions of interest. For 1.5m objects in Figure 8(b), this average percentage drops to

97.1%, 96.5%, and 98.3% for the surveillance cone, lunar exclusion cone, and L_1L_2 sphere, respectively. When the object radius is further reduced to 0.5m in Figure 8(a), the average percentages drop to 57.6%, 73.7%, and 82.8%, respectively. Notable however is that even when $R_{obj} = 0.5m$, on average there is a larger amount of the L_1L_2 sphere that is visible, as many cislunar orbits of interest lie within this region.

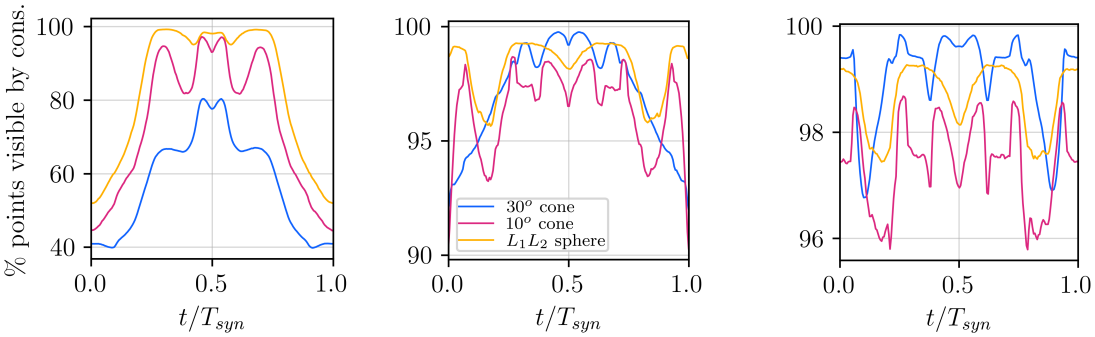

(a) Radius of 0.5m. (b) Radius of 1.5m. (c) Radius of 3.5m.

Figure 8: Visibility of the surveillance cone from a five-spacecraft constellation in a 3:5 synodic 3:2 spatial PC-type sidereal resonant orbit for different object radii with a Lambertian coefficient of $C_d = 0.5$.

The results from the CR3BP analysis that incorporate the coplanar BCR4BP solar position are validated in the HFEM. The initial epoch when transitioning the CR3BP orbit to the HFEM is selected to yield the same planar solar phase angle in the Earth-Moon pulsating-rotating frame as from the lower-fidelity analysis. Figure 9 plots the planar solar phase angle in this pulsating-rotating frame for the first six synodic months of 2026. Positions of the Sun, Earth, and Moon are retrieved from SPICE ephemerides, and details about the rotation of inertial states into the Earth-Moon pulsating-rotating frame are detailed by Park & Howell.[14] For this example, an initial solar phase angle of $\theta_{SB} = 0$ is selected, and this angle is obtained on January 18, 2026 at 20:21:16 UTC. This epoch is the initial epoch employed for the CR3BP to HFEM transition process.

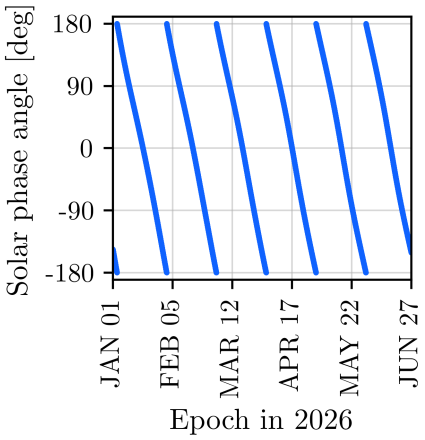

Figure 9: Planar solar phase angle in the Earth-Moon pulsating-rotating frame.

The CR3BP trajectories are transitioned to the HFEM by constructing an initial guess from stacked revolutions of the CR3BP trajectory. As there are five spacecraft in the constellation, five unique trajectories are generated due to the not perfectly periodic motion of the celestial bodies in the J2000 frame. These trajectories are computed with times-of-flight of at least six months, however longer baselines could feasibly be converged. A two-level differential targeting process is employed that yield trajectories that are initially continuous in position only and the trajectories are re-converged by reducing the magnitude of the velocity discontinuities until ballistic paths are produced. An eclipse avoidance path constraint developed in Ojeda-Romero and Howell[19] and

Zimovan-Spreen, Howell, and Davis,[20] and applied to sidereal resonant orbits by Gupta and Howell,[21] is implemented. The ballistic trajectories that emerge do not pass through the Moon and Earth penumbra cones plotted in Figure 10. Strategies exist to seek individual trajectories that are more similar, but they are not pursued here. The Earth and Moon eclipse cones are viewed in Figures 11(a) and 11(b) in the Sun-Earth and Sun-Moon pulsating-rotating frames, respectively, where the red markers denote regions of eclipse. The eclipse avoidance path constraint shifts the orbital paths such that they merely "skim" the penumbra cones. Note that the eclipse point in Figure 11(b) that appears to be inside of the cone actually skims the penumbra cone at a location closer to the Moon where the diameter of the cone at that $\hat{x}_{SM}$ location is smaller than apparent in the projection. Additionally, lines that appear to enter the penumbra cones but are not in eclipse, pass between the Sun and eclipsing body, and therefore, do not pass through the penumbra cones.

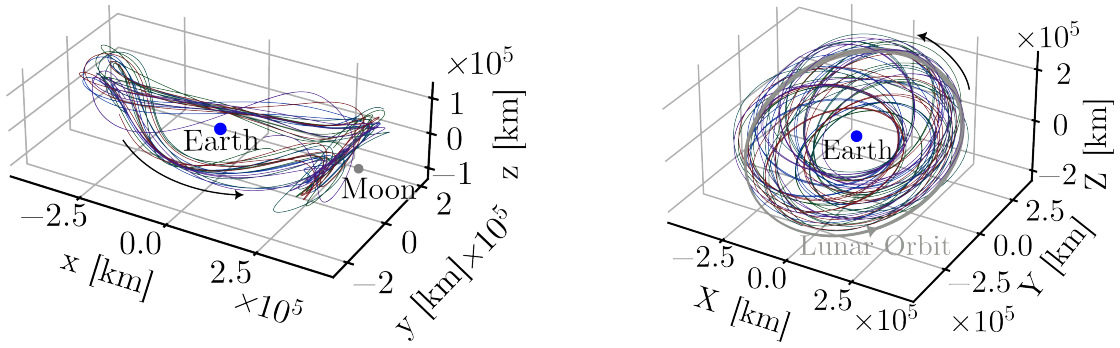

(a) Earth-Moon pulsating-rotating frame.

(b) Earth-centered J2000 frame.

Figure 10: 3:5 synodic spatial PC-type 3:2 sidereal resonant orbit in different frames for the five-spacecraft constellation in the Earth-Moon-Sun-Jupiter HFEM model. All paths are ballistic and eclipse-free with a a minimum time-of-flight of 6 synodic months.

Evaluating the visibility of the points within the surveillance cone from the HFEM trajectories and the Sun location retrieved from ephemerides over six synodic months for objects of radius $R_{obj} = 3.5m$ and the Lambertian coefficient $C_d = 0.5$ yields the results plotted in Figure 12. The percentage visibility for the different zones over the six synodic months is 99.0%, 96.8%, and 98.2%, for the surveillance cone, lunar exclusion cone, and L_1L_2 sphere, respectively. The horizontal axis tick marks are spaced out by 1 synodic month; similar trends for 1 synodic month in the lower-fidelity analysis plotted in Figure 8(c) are thus identified in the higher-fidelity results. This similarity in the visibility results demonstrates that the dominant frequencies that govern this analysis are captured in the lower-fidelity analysis, as even when adding perturbing bodies and their realistic positions in the HFEM, this dominant behavior is maintained.

RESULTS: 3:5 SYNODIC RESONANT 3:2 SIDEREAL PC-TYPE SPATIAL RESONANT ORBIT AND 4:1 SYNODIC RESONANT L_2 HALO ORBIT

Several synodic resonant orbits paired together can improve the visibility of the cone. For this example, the same PC-type orbit as the previous example with a five-satellite constellation is paired with a sixth observer in a 4:1 synodic resonant L_2 halo orbit in the CR3BP. The halo orbit with one spacecraft repeats every synodic period (and in fact, every 1/4 synodic periods), and so the entire six-satellite network maintains its configuration every synodic period as well. Views of the 3:2

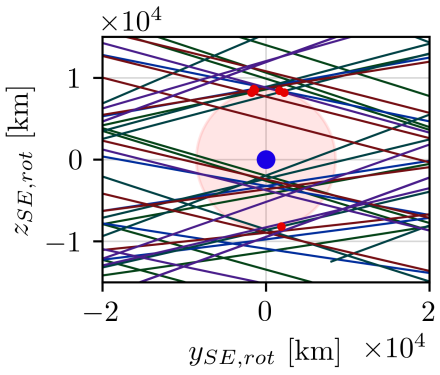

(a) Earth eclipses viewed in the Sun-Earth pulsating-rotating frame

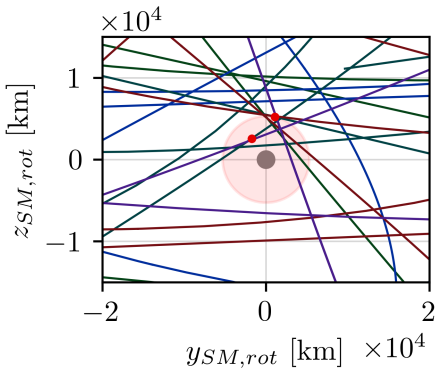

(b) Moon eclipses viewed in the Sun-Moon pulsating-rotating frame

Figure 11: Viewing the PC-type trajectory from different frames after implementing the eclipse avoidance path constraints. Red points identify portions of the trajectory in eclipse and the pink circle is the projection of the penumbra cone at the eclipse location with the largest amplitude position component in the Sun-body direction.

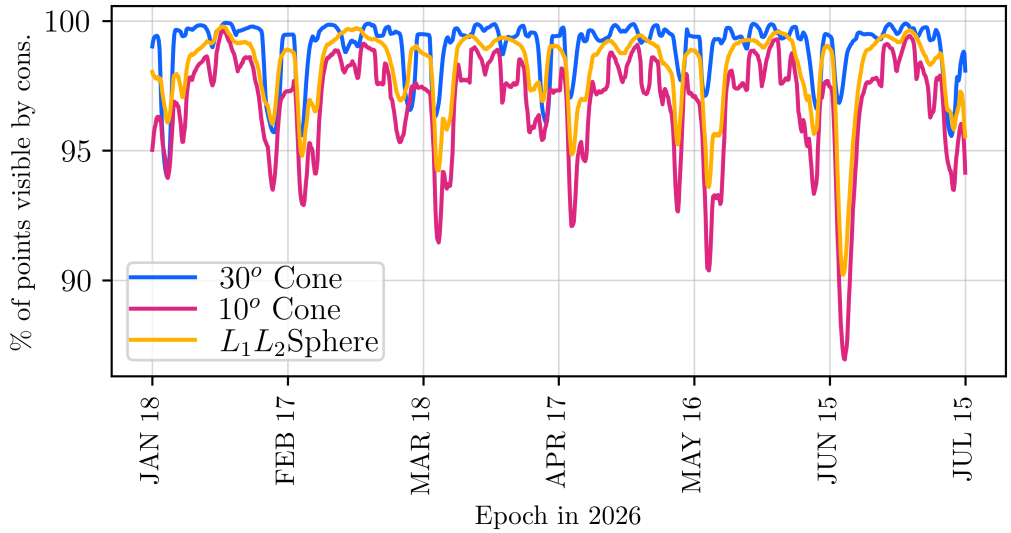

Figure 12: Visibility analysis for the ballistic and eclipse-free HFEM trajectories displayed in Figure 10, $R_{obj} = 3.5m, C_d = 0.5$.

resonant orbit and the halo orbit relative to the surveillance cone in the CR3BP rotating frame are displayed in Figure 13, where the halo orbit notably possesses a very small set of vantage points and, even with multiple observers, does not offer significantly different points of view. For this reason, the initial phase of the sixth observer along the halo does not significantly impact the results; for this constellation, this observer initially possesses an encoding angle of $\theta_{enc} = 0$ and remains in the L_1L_2 sphere at all times.

The percentage of points visible in the regions of interest from this two-orbit, six-satellite constellation is plotted in Figure 14. The same set of object radii are examined: $R_{obj} = 0.5m, 1.5m, 3.5m$.

In these plots, the solid lines represent the percentage visibility when including only the 3:2 sidereal resonant, i.e., they describe the same results as Figure 8 with only five observers. The dashed lines reflect the six-spacecraft constellation that incorporates the observer in the halo orbit. For the largest radius with results plotted in Figure 14(c), the average percentage of points in the cone that are visible by the constellation is 99.3%, 99.1%, and 99.7% for the surveillance cone, lunar exclusion cone, and L_1L_2 sphere, respectively. For the $R_{obj} = 1.5m$ objects in Figure 14(b), these average percentages are 97.6%, 98.7%, and 99.7% for those same respective regions. Finally, for the smallest $R_{obj} = 0.5m$ objects in Figure 14(a), the average percentages are, respectively, 65.9%, 84%, and 93.7%. This additional observer notably improves the visibility of the L_1L_2 sphere, especially for smaller object radii. Recall that for the five-spacecraft constellation in the 3:2 resonant orbit, the average percentage of points visible in the L_1L_2 sphere for $R_{obj} = 0.5m$ is 82.8%, compared to 93.7% with the additional observer in the halo orbit.

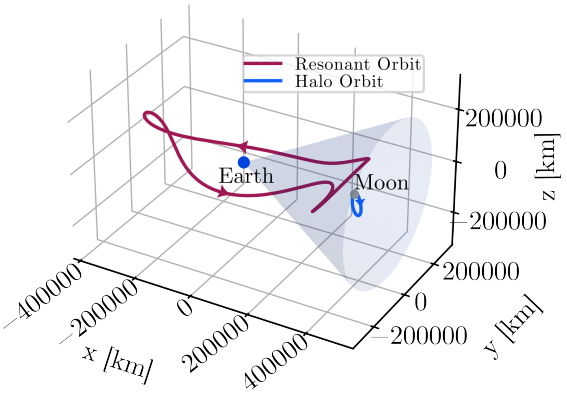

Figure 13: 3:5 synodic resonant 3:2 spatial PC-type sidereal resonant orbit and a 4:1 synodic L_2 halo orbit

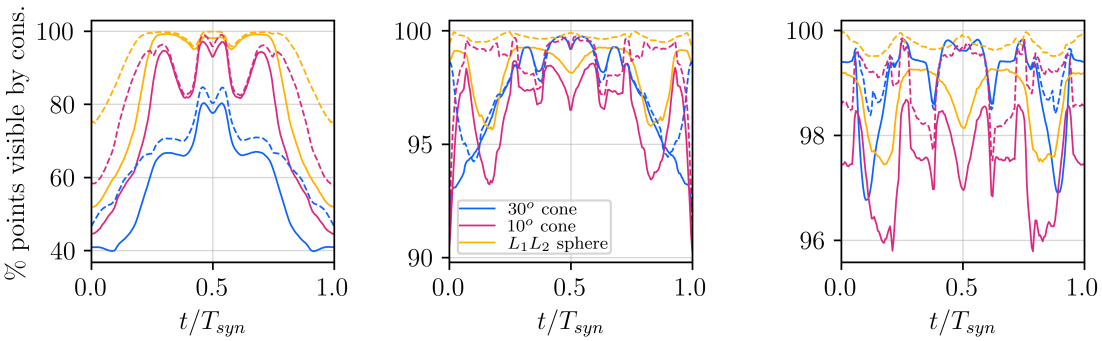

(a) Radius of 0.5m. (b) Radius of 1.5m. (c) Radius of 3.5m.

Figure 14: Visibility of the surveillance cone from a five-spacecraft constellation in a 3:5 synodic 3:2 spatial PC-type sidereal resonant orbit paired with an additional observer in a 4:1 synodic L_2 halo orbit for different object radii with a Lambertian coefficient of $C_d = 0.5$. The solid lines are the percentages incorporating only the 3:2 resonant orbit constellation and the dashed lines reflect adding the observer in the halo orbit to the constellation.

RESULTS: 3:5 SYNODIC RESONANT 3:2 SIDEREAL AC-TYPE SPATIAL RESONANT ORBIT

The 3:2 spatial sidereal AC-type resonant orbit family is also identified as possessing repeating geometries with varied vantage points for observing this cislunar region of interest. Specifically with the 3:2 spatial sidereal AC-type family, the 3:5 synodic resonant member of the family, plotted in Figure 15, supports a five-spacecraft synodic resonant constellation that returns to the initial configuration after every synodic period. This orbit is also linearly unstable, with a time constant similar

to the 3:2 spatial sidereal PC-type resonant orbit with 3:5 synodic resonance of $\kappa_T = 2.8986nd$ or approximately 12.60 days. For this constellation, the initial solar phase angle is selected as 180 degrees and one spacecraft is initially placed at an encoding angle of zero. The visibility of the points within the surveillance cone are analyzed for one synodic period, with the resulting percentage of points visible within each region over that interval plotted in Figure 16 for object radii of 0.5m, 1.5, & 3.5m, and a Lambertian coefficient of $C_d = 0.5$. For objects of radius $R_{obj} = 3.5m$ in Figure 16(c), the percentage of points visible by the constellation for the entire surveillance cone, lunar exclusion cone, and L_1L_2 sphere are 99.1%, 98.3%, and 98.7%, respectively. Reducing the radius to $R_{obj} = 1.5m$ in Figure 16(b), these respective percentages drop to 91.8%, 95.4%, and 97.9%. For the smallest considered radius of $R_{obj} = 0.5m$ in Figure 16(a), these respective percentages are notably smaller, i.e., 50.2%, 70.5%, and 76.1%. These percentages are lower than in the PC-type example in the previous section, however, this orbit remains a potential option pairing with other orbits for cislunar surveillance cone observations.

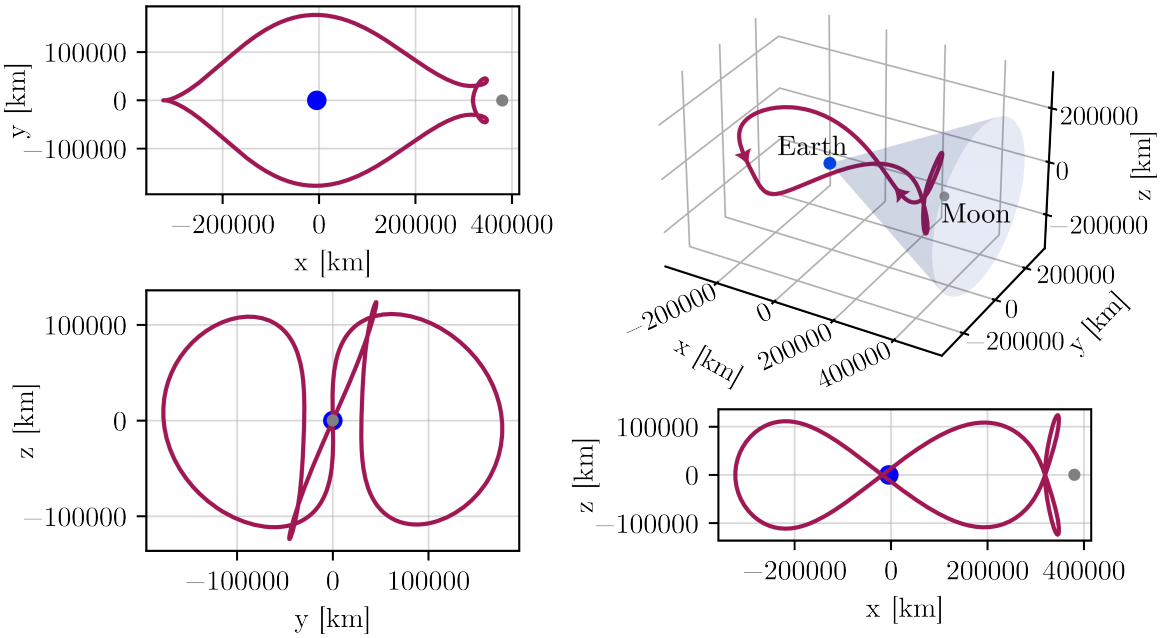

Figure 15: Views of the 3:5 synodic resonant 3:2 spatial AC-type sidereal resonant orbit in the Earth-Moon CR3BP rotating frame. The surveillance cone is highlighted in the top-right isometric view.

The five-spacecraft constellation is transitioned to the HFEM and, as the initial solar phase angle for the lower-fidelity analysis is $\theta_{SB} = 180^o$, an initial epoch of April 2, 2026 at 01:57:05 UTC is selected from Figure 9. The same transition process is employed, and the resulting ballistic and eclipse-free trajectories for all five observers in the constellation over a time-of-flight that spans at least six synodic months are plotted in Figure 17. The projections into the Sun-Earth and Sun-Moon frames normal to the penumbra eclipse cones are displayed in Figure 18, where the converged trajectories skim the eclipse cones, as expected after convergence with the eclipse avoidance path constraint implemented.

Finally, the points within the surveillance cone are evaluated for their visibility from the constellation converged in the HFEM over six synodic months for objects of radius $R_{obj} = 3.5m$ and

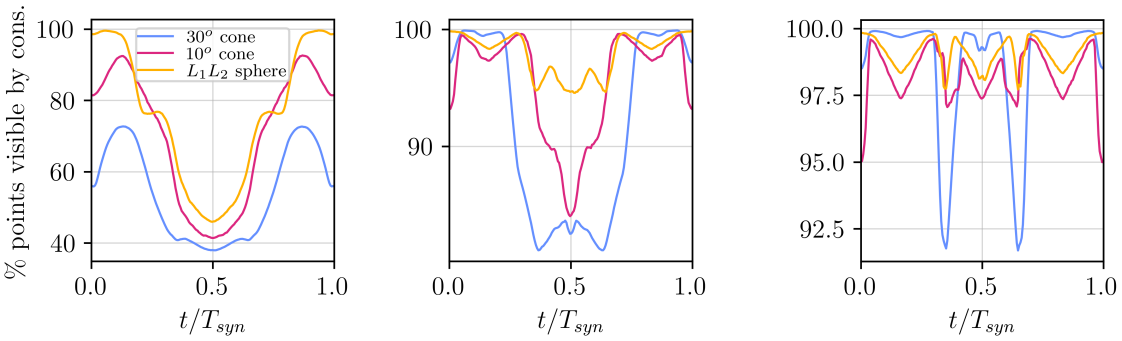

(a) Radius of 0.5m (b) Radius of 1.5m (c) Radius of 3.5m

Figure 16: Visibility of the surveillance cone from a five-spacecraft constellation in a 3:2 spatial AC-type sidereal resonant orbit possessing a 3:5 synodic resonance ratio for different object radii with a Lambertian coefficient of $C_d = 0.5$

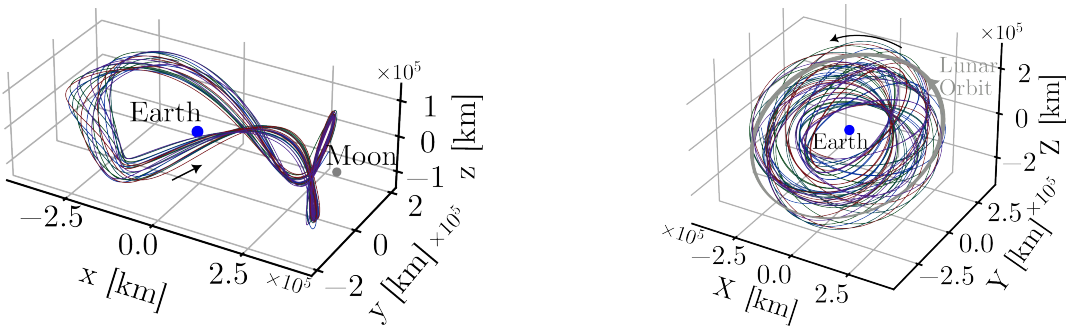

(a) Earth-Moon pulsating-rotating frame (b) Earth-centered J2000 frame

Figure 17: 3:5 synodic spatial AC-type 3:2 sidereal resonant orbit in different frames for the five-spacecraft constellation in the Earth-Moon-Sun-Jupiter HFEM model. All paths are ballistic and eclipse free with a minimum time-of-flight of 6 synodic months.

a Lambertian coefficient of $C_d = 0.5$. The variation in percentage of points visible by the constellation exhibits repeatable patterns every synodic period that are similar to the synodic-month lower-fidelity analysis plotted in Figure 16(c). The average percent visibility by the constellation is 98.5%, 98.3%, and 99.1% for the surveillance cone, lunar exclusion cone, and L_1L_2 sphere, respectively, and reasonably consistent with the values obtained in the lower-fidelity analysis. This similarity highlights the advantage of analyzing the visibility of the surveillance cone from a constellation by employing a lower-fidelity model to evaluate the feasibility of a particular constellation before conducting a computationally-intensive HFEM analysis.

SUMMARY

Sidereal resonant orbits possessing a synodic resonance overlap are identified as useful baseline orbits for constellations of satellites to observe the cislunar surveillance cone for space situational awareness applications. Constellations of observer spacecraft equally-spaced in time along these orbits such that the configuration is maintained every synodic period are analyzed for one synodic month to inform on their long-term visibility trends. Visibility is quantified by sampling a number

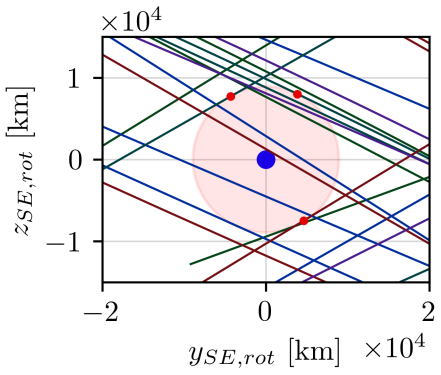

(a) Earth eclipses viewed in the Sun-Earth pulsating-rotating frame.

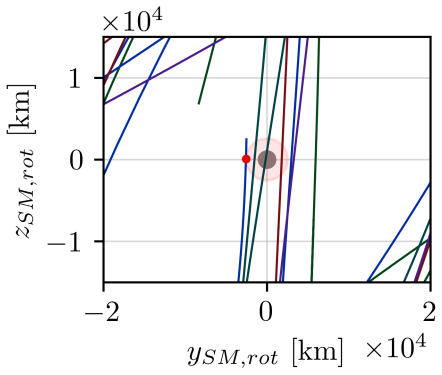

(b) Moon eclipses viewed in the Sun-Moon pulsating-rotating frame.

Figure 18: Viewing the HFEM 3:5 synodic spatial AC-type 3:2 sidereal resonant orbit trajectories from different frames after implementing the eclipse avoidance path constraints. Red points identify portions of the trajectory in eclipse and the pink circle is the projection of the penumbra cone at the eclipse location with the largest amplitude position component in the Sun-body direction.

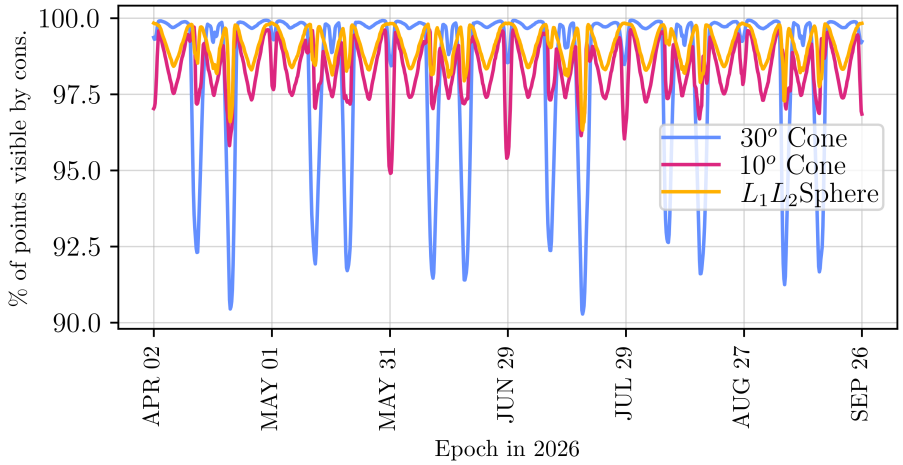

Figure 19: Visibility analysis for the ballistic and eclipse-free HFEM AC-type trajectories displayed in Figure 17. $R_{obj} = 3.5m, C_d = 0.5$.

of points inside the surveillance cone and assessing the potential for the points to be visible from a constellation of satellites on a common orbit; the criteria for visibility includes (i) the relative magnitude of the points and (ii) whether they lie in the spacecraft solar, lunar, or earth exclusion cones. Two commonly-used relative magnitude model formulations are examined, and the choice of model selection significantly affects the number of visible points, especially when considering smaller objects. Cislunar space observations from space-based observers, therefore, also requires a careful understanding of the photometric properties of objects being observed.

Several modeling frameworks are employed in this investigation. The CR3BP is leveraged to permit a lower-fidelity analysis where the solar position is obtained from the coplanar BCR4BP. In this framework, and when using synodic resonant orbits, the visibility analysis occurs over a single

synodic period and, therefore, long-term behavior is inferred from this short-term analysis, greatly reducing the computational cost. Solutions from this lower-fidelity formulation are transitioned to a higher-fidelity ephemeris model, and the general behavior predicted by the CR3BP+BCR4BP analysis exist and demonstrates approximate synodic resonance as well. As the computational cost associated with the HFEM analysis is higher than the CR3BP+BCR4BP analysis, the lower-fidelity formulation serves to as a basis to assess the feasibility of a particular constellation before validating these results in the HFEM.

The PC-type and AC-type 3:2 sidereal resonant orbit families are sample scenarios to demonstrate pairing orbits for an observing constellation, as these families possess geometries that offer varied vantage points for observations of the surveillance cone and, with apses in the cone, spacecraft linger near the region of interest. Specifically, the 3:5 synodic resonant members of these families and a five-spacecraft constellation are employed. Both the AC-type and PC-type geometries observe nearly the entire surveillance cone, on average, when focused on large objects, implying few overlaps of exclusion cones for the constellation. For smaller objects, the relative magnitude cutoff reduces the visibility of the surveillance cone. A PC-type resonant constellation, paired with an observer in a 4:1 synodic L_2 halo orbit, improves the visibility within the cone, with notable improvements for smaller objects in the L_1L_2 sphere.

ACKNOWLEDGEMENTS

The authors gratefully acknowledge support for this research from the Air Force Office of Scientific Research (AFOSR), in particular Dr. Stacie Williams, as part of the Space University Research Initiative (SURI), grant FA95502210092. Financial support from the *Fonds de Recherche du Québec – Nature et Technologies* through grant number 332821 and the National Science and Engineering Research Council of Canada through grant number PGSD-578418 is also appreciated. Special thanks to Juan-Pablo Almanza-Soto for suggesting the torus visualization for synodic resonant orbits, as well as to Surabhi Bhadauria for insights into the relative magnitude models. Finally, insightful discussions with colleagues in the Purdue Multi-Body Dynamics Research Group were greatly appreciated.

REFERENCES

[1] "National cislunar science & technology strategy," tech. rep., National science & technology council, cislunar technology strategy interagency working group, Nov. 2022.
[2] "Space Domain Awareness," Tech. Rep. SDP 3-100, Space Training and Readiness Command, Nov. 2023.
[3] M. Gupta, K. C. Howell, and C. Frueh, "Earth-Moon Multi-Body Orbits to Facilitate Cislunar Surveillance Activities," *AAS/AIAA Astrodynamics Specialist Conference*, Big Sky, MT (Virtual), Aug. 2021.
[4] J. J. Roth and E. J. Felt, "Overcoming Technical Challenges from Low Earth Orbit to Cislunar," Presentation at the 2020 AMOS conference, Sept. 2020.
[5] F. Conner, "AFRL's Oracle Family of Systems Developing Nation's 1st Cislunar Space Situational Awareness Capabilities," Dec. 2023. https://www.afrl.af.mil/News/Article-Display/Article/3611977/afrls-oracle-family-of-systems-developing-nations-1st-cislunar-space-situationa/, last accessed 2024-04-09.
[6] M. J. Holzinger, C. C. Chow, and P. Garretson, "A Primer on Cislunar Space," 2021.
[7] J. K. Vendl and M. J. Holzinger, "Cislunar Periodic Orbit Analysis for Persistent Space Object Detection Capability," *Journal of Spacecraft and Rockets*, Vol. 58, July 2021, pp. 1174–1185, doi/org/10.2514/1.A34909.
[8] S. Bhadauria, C. Frueh, and K. Howell, "Cislunar Space Domain Awareness Using Bi-Circular Four Body Geometry," *AAS/AIAA Astrodynamics Specialist Conference*, Charlotte, NC, Aug. 2022.
[9] M. Gupta, K. C. Howell, and C. Frueh, "Constellation Design to Support Cislunar Surveillance Leveraging Sidereal Resonant Orbits," *AAS/AIAA Astrodynamics Specialist Conference*, Big Sky, MT, Aug. 2023.

[10] M. Gupta, *Navigating Chaos: Resonant Orbits for Sustaining Cislunar Operations*. PhD dissertation, Purdue University, West Lafayette, USA, May 2024.
[11] L. Visonneau, Y. Shimane, and K. Ho, "Optimizing Multi-Spacecraft Cislunar Space Domain Awareness Systems via Hidden-Genes Genetic Algorithm," *The Journal of the Astronautical Sciences*, Vol. 70, July 2023, p. 22, doi.org/10.1007/s40295-023-00386-8.
[12] B. Baker-McEvilly, S. Bhadauria, J. Rose, D. Canales Garcia, C. Frueh, and H. Cho, "Performance of Observational Spacecraft Across Orbit Families for Space Domain Awareness in the Cislunar Realm," *AIAA Scitech 2024*, Orlando, FL, Jan. 2024, doi.org/10.2514/6.2024-2067.
[13] S. Scheuerle, *Low-Energy Transfers in the Bicircular Restricted Four-Body Problem*. PhD dissertation, Purdue University, West Lafayette, USA, May 2024.
[14] B. Park and K. C. Howell, "Assessment of dynamical models for transitioning from the Circular Restricted Three-Body Problem to an ephemeris model with applications," *Celestial Mechanics and Dynamical Astronomy*, Vol. 136, Feb. 2024, p. 6, doi.org/10.1007/s10569-023-10178-9.
[15] R. S. Park, W. M. Folkner, J. G. Williams, and D. H. Boggs, "The JPL Planetary and Lunar Ephemerides DE440 and DE441," *The Astronomical Journal*, Vol. 161, Mar. 2021, doi.org/10.3847/1538-3881/abd414.
[16] C. H. Acton, "Ancillary data services of NASA's Navigation and Ancillary Information Facility," *Planetary and Space Science*, Vol. 44, Jan. 1996, pp. 65–70, doi.org/10.1016/0032-0633(95)00107-7.
[17] C. Acton, N. Bachman, B. Semenov, and E. Wright, "A look towards the future in the handling of space science mission geometry," *Planetary and Space Science*, Vol. 150, Jan. 2018, pp. 9–12, doi.org/10.1016/j.pss.2017.02.013.
[18] A. M. Annex, B. Pearson, B. Seignovert, B. T. Carcich, H. Eichhorn, J. A. Mapel, J. L. F. v. Forstner, J. McAuliffe, J. D. d. Rio, K. L. Berry, K.-M. Aye, M. Stefko, M. d. Val-Borro, S. Kulumani, and S.-y. Murakami, "SpiceyPy: a Pythonic Wrapper for the SPICE Toolkit," *Journal of Open Source Software*, Vol. 5, Feb. 2020, p. 2050, doi.org/10.21105/joss.02050.
[19] J. A. Ojeda Romero and K. C. Howell, "Ridesharing Options from Geosynchronous Transfer Orbits to the Sun–Earth L1 Region," *Journal of Spacecraft and Rockets*, Vol. 60, Mar. 2023, pp. 601–615. Publisher: American Institute of Aeronautics and Astronautics, doi.org/10.2514/1.A35485.
[20] E. M. Zimovan-Spreen, K. C. Howell, and D. C. Davis, "Dynamical Structures Nearby NRHOs with Applications to Transfer Design in Cislunar Space," *The Journal of the Astronautical Sciences*, Vol. 69, June 2022, pp. 718–744, 10.1007/s40295-022-00320-4.
[21] M. Gupta and K. C. Howell, "Cislunar Eclipse Mitigation Strategies for Resonant Periodic Prbits," *AAS/AIAA Astrodynamics Specialist Conference*, Big Sky, MT, Aug. 2023.
[22] E. Zimovan-Spreen, *Trajectory Design and Targeting for Applications to the Exploration Program in Cislunar Space*. PhD dissertation, Purdue University, West Lafayette, USA, May 2021.
[23] R. J. Gomez, J.-P. Almanza-Soto, K. C. Howell, and J. D. Aziz, "Construction and Analysis of "L1/L2" Cycler Orbits in the Earth-Moon System," *AAS/AIAA Astrodynamics Specialist Conference*, Big Sky, MT, Aug. 2023.
[24] C. D. Murray and S. F. Dermott, *Solar System Dynamics*. Cambridge: Cambridge University Press, 2000, doi.org/10.1017/CBO9781139174817.
[25] N. I. Sadaka and K. C. Howell, "Periodic Transfers that Depart and Return to an Operating Orbit Using Resonant Orbit Structures in the Planar Three-Body Problem," *33rd AAS/AIAA Space Flight Mechanics Meeting*, Austin, TX, Jan. 2023.
[26] N. B. LaFarge, K. C. Howell, and D. C. Folta, "Adaptive closed-loop maneuver planning for low-thrust spacecraft using reinforcement learning," *Acta Astronautica*, Vol. 211, 2023, pp. 142–154, doi.org/10.1016/j.actaastro.2023.06.004.
[27] E. D. Silva, J. V. Cleve, R. Philbrick, C. J. Grant, J. D. Griesbach, and M. P. Mahoney, "System and Methods for Hybrid Lunar Surface and Space Domain Situational Awareness," *AMOS 2021 Conference*, Maui, HI, 2021.
[28] D. A. Vallado, M. R. Ackermann, P. J. Cefola, and R. R. Kiziah, "Orbital Strategies to Mitigate the Solar Exclusion Effect on Space-Based Observation of the Geosynchronous Belt," *2016 AIAA/AAS Astrodynamics Specialist Conference*, Sept. 2016, doi.org/10.2514/6.2016-5433.
[29] C. Frueh, B. Little, and J. McGraw, "Optical Sensor Model and its Effects on the Design of Sensor Networks and Tracking," *Advanced Maui Optical and Space Surveillance Technologies Conference*, Maui, HI, Sept. 2019.
[30] C. Frueh, "AAE590 – Space Traffic Management," Aug. 2023. Course notes. Version 6.0. Purdue University, School of Aeronautics and Astronautics.
[31] J. R. Shell, "Optimizing orbital debris monitoring with optical telescopes," *AMOS 2010 Conference*, Maui, HI, 2010.
[32] R. J. Power, "Characterization of Lunar Access Relative to Cislunar Orbits," M.S. thesis, Purdue University, West Lafayette, USA, Dec. 2019.